We are IntechOpen, the world's leading publisher of Open Access books Built by scientists, for scientists

4,800
Open access books available

122,000
International authors and editors

135M
Downloads

Our authors are among the

154
Countries delivered to

TOP 1%
most cited scientists

12.2%
Contributors from top 500 universities

WEB OF SCIENCE™

Selection of our books indexed in the Book Citation Index in Web of Science™ Core Collection (BKCI)

Interested in publishing with us?
Contact book.department@intechopen.com

Numbers displayed above are based on latest data collected.
For more information visit www.intechopen.com

10

Large Scale Graphene by Chemical Vapor Deposition: Synthesis, Characterization and Applications

Lewis Gomez De Arco, Yi Zhang and Chongwu Zhou
University of Southern California
USA

1. Introduction

Faster and smaller computers, smarter medicaments, ultrasensitive sensors, dreams of a new generation of products that are increasingly cleaner, lighter, stronger and more efficient; those are aspects that represent the aspirations of a great part of human kind that ever more strives for better technologies. Interestingly, the concept of nanotechnology is at the center of this discussion. Nanotechnology has become instrumental on finding pathways to arrive to processes and products that are not only needed today but will become essential in the future.

Nanotechnology can be defined as the understanding and manipulation of matter with at least one dimension of the order of 1 to 100 nanometers, where unique phenomena enable novel applications. For example, whereas elemental carbon is a poor conductor of electricity and not particularly strong, the two-dimensional carbon is a semimetal that exhibits high charge carrier mobility, obeying the laws of relativistic rather than regular quantum mechanics. Furthermore, one-dimensional carbon has mechanical strength 100 times higher than steel, exhibiting either metallic or semiconducting properties depending on their chiral atomic arrangement. Two principal factors cause nanomaterials properties to differ significantly from bulk materials: increased relative surface area, which can change or enhance chemical reactivity (Arenz, Mayrhofer et al. 2005); and quantum effects that can affect the material optical, magnetic and electrical properties (Yu, Li et al. 2003). It is precisely the collection of new and surprising properties of nanomaterials what has motivated the scientific and engineering community to invest a tremendous share of effort towards a better understanding of their physical and chemical properties; as well as finding controllable synthesis and accurate characterization techniques.

Graphene sheets are one-atom thick, 2D layers of sp^2-bonded carbon. It is interesting that carbon with sp^2 hybridization is able to form the two-dimensional graphene, the planar local structure in the closed polyhedral of the fullerene family and the cylinder-shaped carbon nanotubes, all with different physical properties (see table 1). Thus, keeping the sp^2 hybridization, the 2D carbon can be wrapped up into 0D fullerenes, rolled into 1D nanotubes, or stacked into 3D graphite.

Carbon has four electrons in its valence level with a configuration of $2s^22p^2$. The hexagonal structure of graphene poses an alternate double bond arrangement that makes it perfectly conjugated in sp^2 hybridization. In this case its p_x and p_y orbitals contain one electron each, and the remaining p_z has only one electron. This p_z orbital overlaps with the p_z orbital of a

neighbor carbon atom to form a π-bond, while the remaining orbitals form σ-bonds with other neighboring carbons. π-electrons in graphene are delocalized and are largely responsible for its conduction properties, while π-orbitals are the most important for determining the solid state properties of graphene.

Dimension	0-D	1-D	2-D	3-D
Isomer	Fullerene	Nanotube	Graphene	Diamond
Hybridization	sp^2	sp^2	sp^2	sp^3
Density	1.72	1.2-2.0	2.26	3.515
Bond length	1.40 (C=C) 1.46 (C-C)	1.44 (C=C)	1.42 (C=C)	1.54 (C-C)
Electronic properties	Semiconductor E_g=1.9 eV	Metal/Semiconductor Eg= ~0.3 – 1.1 eV	Zero-gap semiconductor	Insulator

Table 1. Important parameters of carbon materials of different dimensionalities

One of the greatest concerns on graphene research since 1934 was the idea that a strictly two-dimensional crystal could not freely exist, some studies had concluded that these crystals were thermodynamically unstable (Mermin 1968) and it was established that in the standard harmonic approximation, thermal fluctuations will destroy long-range order, resulting in melting of a 2D lattice. It was also presumed that during synthesis, any graphene nucleation sites will have large perimeter-to-surface ratios, thus favoring the formation of other carbon allotropes instead of graphene. Despite the odds, a breakthrough discovery reported only recently demonstrated graphene isolation at ambient conditions (Novoselov, Geim et al. 2004).

Graphene is formed by a two-dimensional hexagonal arrangement of carbon atoms with a quasi-linear dispersion relation, for which the carrier effective mass is very low (Zhang, Tan et al. 2005). As a consequence, it has a predicted mobility at room temperatures in the order of 10^6 cm^2/Vs and an experimentally measured mobility of 15,000 cm^2/Vs. The high mobility of this material opens the possibility of ballistic transport at submicron scales (Hwang, Adam et al. 2007). The problem, however, is the mass-production of graphene. The technique of choice for the great majority of researchers is the mechanical exfoliation of graphene flakes from graphite and that method is able to produce only research-size graphene samples. The scientific community is employing a lot of effort in the development of technologies for mass production of graphene; such development will constitute a gigantic step forward for graphene-based nano- and macro-electronics.

Numerous methods have been proposed to obtain single-layer or few-layer graphene (FLG) at large scale (Forbeaux, Themlin et al. 1998; Viculis, Mack et al. 2003; Wu, Chen et al. 2004; Gilje, Han et al. 2007), however, the methods proposed so far either not scalable, produce thick graphite, or highly defective graphene layers, or the cost of graphene production is so high that it becomes prohibitive for mass production. In this chapter we present the development of a scalable graphene synthesis method based on chemical vapor deposition, characterization techniques and applications in nano- and macroelectronics. In particular, aspects such as the substrate atomic arrangement on the structure and properties of the synthesized graphene, the evaluation of its electrical properties as the active channel in field effect transistors, and the implementation of the highly scalable graphene synthesized by CVD as the transparent electrode in photovoltaic devices will be amply discussed.

2. Synthesis of large scale graphene by chemical vapor deposition

Despite the advances in graphene research, and the numerous foreseen important applications, implementation of graphene has been hampered due to the difficulty of producing single or few-layer specimens over large areas. Three main methods have been used to obtain single-layer or few-layer graphene (FLG): i) Epitaxial growth of graphene obtained on 6H oriented SiC by vacuum annealing at 1400°C (Forbeaux, Themlin et al. 1998), with the drawback of being limited by the cost and size of SiC substrates; ii) Micromechanical exfoliation of small mesas of highly oriented pyrolytic graphite (HOPG) (Novoselov, Geim et al. 2004), which cannot be scaled to wafer-size dimensions, and iii) chemically-assisted exfoliation of intercalated graphite compounds (Viculis, Mack et al. 2003; Gilje, Han et al. 2007; Wu, Becerril et al. 2008), which typically leads to graphene with large amount of defects. An alternative way is the chemical vapor deposition (CVD) of camphor on nickel (Somani, Somani et al. 2006), which leads to growth of graphene of about twenty layers. Segregation of graphene on Ni surfaces was reported; however, several layers were obtained instead of single-layer graphene, and the electronic properties of the synthesized material were not evaluated (Yu, Lian et al. 2008). Approaches that provide high-quality single- and few-layer graphene over large areas is instrumental to meet realistic applications.

2.1 Apparatus

Chemical vapor deposition is a simple, scalable and cost-efficient method to prepare single and few-layer graphene films on various substrates; it opens a new route to large-area production of high-quality graphene films for practical applications. Figure 1 shows our typical chemical vapor deposition system for graphene synthesis; ultra high purity gases, mass flow controllers (MFCs), a high temperature tube furnace, and pressure control systems are at the heart of the synthesis apparatus. Evaporated Ni film on SiO_2/Si wafers or copper foils are ideal substrates for graphene synthesis. Complete wafer racks of Ni coated Si/SiO_2 substrates as well as rolled up copper foils can be loaded into the quartz tube for graphene synthesis (Figure 2). Under this configuration, wafer and foil sizes are limited only by the tube furnace dimensions, for which large scale graphene can be easily achieved.

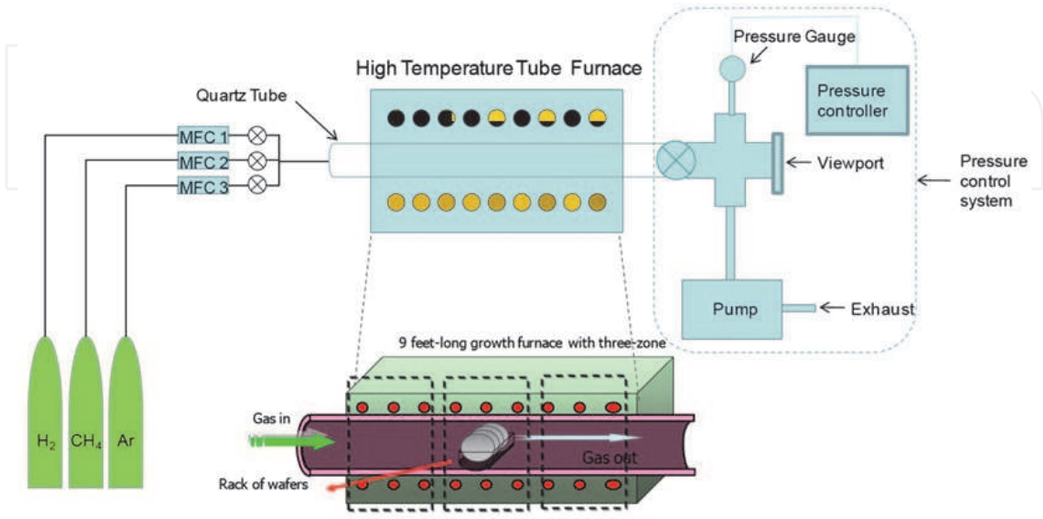

Fig. 1. Complete apparatus setup for chemical vapor deposition of graphene.

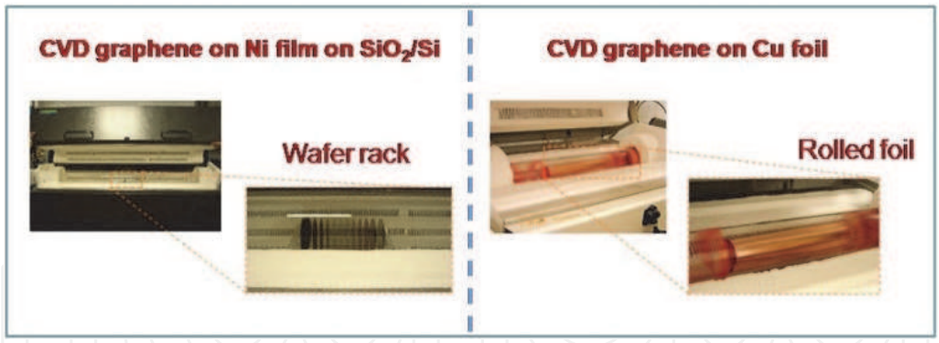

Fig. 2. $Ni/SiO_2/Si$ wafers and copper foils are loaded in the CVD graphene system

Synthesis of graphene on Ni supported on Si/SiO_2 wafers facilitated the breakthrough approach for large scale graphene (Gomez, Zhang et al. 2009); particularly because Ni films provide an excellent geometrical fit of the ordered graphene/graphite phase of carbon to the crystalline metal surface (Zhang, Gomez et al.), as well as convenient interactions that favor bond formation between carbon atoms at specific conditions (Eizenberg and Blakely 1979). It is assumed that the carbon atoms dissolve into the Ni crystalline surface, and at certain temperatures, they arrange epitaxially on the Ni (111) surface to form graphene (figure 3). Synthesized graphene films on Ni were recovered on Si/SiO_2 substrates for device fabrication. In addition, we have achieved transferring the as-synthesized films to different target substrates such as Si/SiO_2 and glass; which may enable wafer-scale silicon-compatible fabrication of hybrid silicon/graphene electronics and transparent conductive film applications.

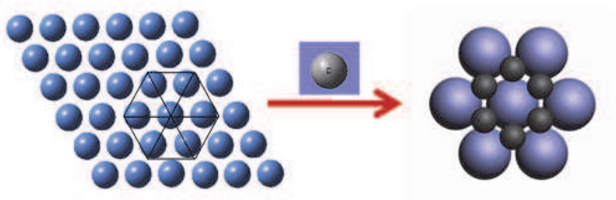

Fig. 3. Schematic representation of the atomic arrangement of the hexagonal lattice of the (111) face of nickel (blue spheres) and how carbon atoms (gray spheres) would arrange on the Ni (111) surface to form graphene.

2.2 Synthesis of graphene by chemical vapor deposition

In a typical synthesis procedure, Si/SiO_2 wafers of 4 inch in diameter were used as substrates to deposit 100 nm thick films of elemental Ni by electron beam (e-beam) evaporation of an elemental Ni target with purity 99.999%. Evaporated films were annealed at 300 or 800 °C in a 10:1 $Ar:H_2$ mixture to induce the formation of polycrystalline nickel on the substrate surface. CVD synthesis of graphene can be carried out at ambient pressure or vacuum by systematically varying parameters such as temperature, gas composition, gas flow rate and deposition time (Gomez, Zhang et al. 2009). We found that using diluted methane was key for the growth of single and few-layer graphene (less than 5 layers), while using concentrated methane leads to the growth of multilayer graphene instead of single or few-layer graphene. This graphene growth method can be extended to other carbon precursors such as ethylene, acetylene, ethanol, and isopropanol, and other metallic films.

2.3 CVD graphene characterization

2.3.1 X-ray diffraction of high-temperature annealed Ni film

X-ray diffraction spectra were collected on the annealed Ni substrates over which graphene films are typically synthesized. Figure 4a shows an AFM image of a typical 1000 Å thick polycrystalline Ni surface. The observed irregular and faceted-shape surface is consistent with polycrystalline surface arrangement. X-ray diffraction spectrum shown in Figure 4b reveals the presence of (111) and (200) planes; being the (111) plane clearly dominant.

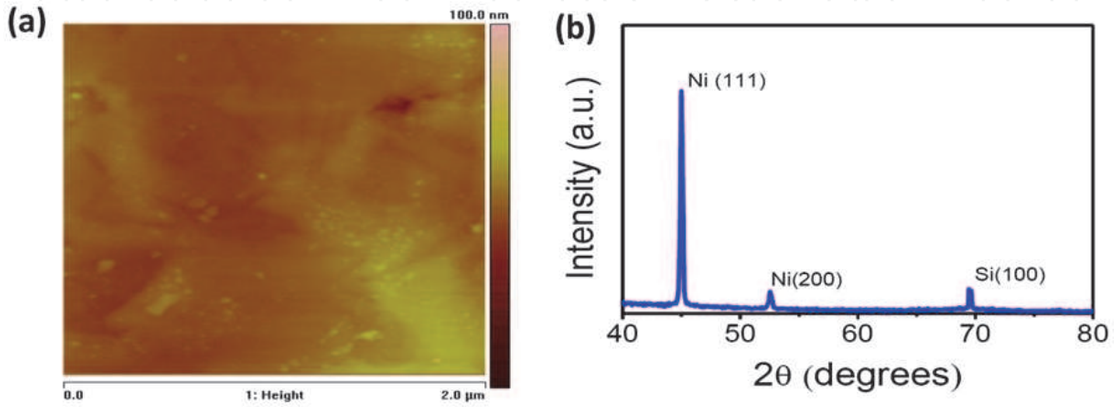

Fig. 4. (a) AFM image of a 300 nm Ni film deposited on Si/SiO2 substrate after high temperature annealing. (b) Typical X-ray diffraction spectrum of annealed Ni film.

2.3.2 AFM, TEM and SAED of CVD graphene

Cross section analysis of AFM images taken on transferred CVD graphene on glass substrates allows a quantitative estimate of the film thickness. Figure 5a shows an AFM image of an opening in the graphene film with clear edges. Figure 5b shows the height profile along the straight line depicted in Figure 5a. A height step of ~1nm can be clearly observed between the substrate surface and the graphene film. Because transferred graphene may not attach perfectly flat on the receiving substrate due to mechanical distortions, in-plane film compression or film folding, the lowest vertical distance within the AFM profile edge steps can be regarded as a good estimate of the film thickness. In this case, a thickness of ~1 nm indicates the CVD graphene can be as thick as bilayer graphene. Figure 5c shows a high resolution TEM image of a typical graphene film obtained by CVD. In order to confirm the thickness of the graphene film, we focused in wrinkle-like regions such as the one shown in the dotted box in figure 5c. It is clearly seen from the magnified image that the cross section of the wrinkle shows two adjacent layers of graphene, which indicates that the graphene film is composed by either wrinkled single layer graphene or stacked graphene bilayer. This result is outstanding; even more considering that the extent of single layer graphene that can be obtained by CVD technology has the potential of producing meter-sized graphene films and the percentage of single layer graphene in the films obtained can be higher than 95%. The inset of Figure 5c presents the typical selected area electron diffraction (SAED) pattern along the z-direction. The hexagonal diffraction pattern indicates a well ordered graphene lattice structure.

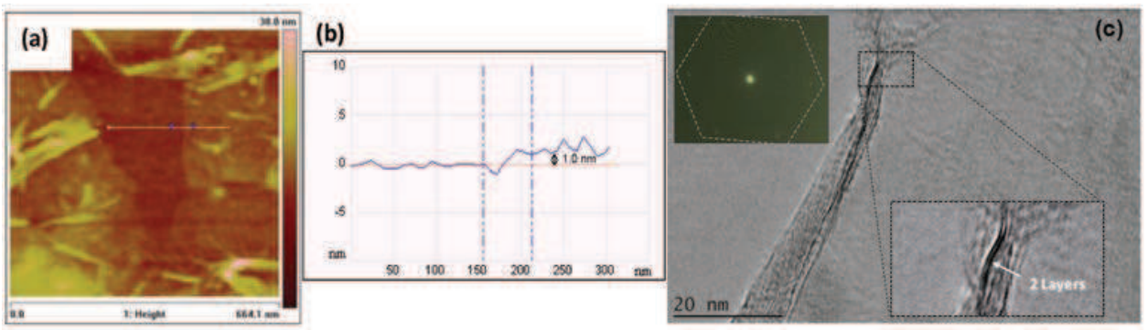

Fig. 5. (a) AFM image of a transferred CVD graphene film onto glass substrate. (b) Cross section measurement of the height of the CVD graphene. Typical thickness exhibited by the transferred films is found within the range 1-3 nm. (c) TEM image of CVD graphene films. Inset shows a selected area electron diffraction (SAED) pattern typical of graphene (hexagonal dotted lines are used to guide the eye).

2.3.3 Micro Raman characterization of CVD graphene

Micro Raman analysis is a powerful tool to confirm the formation of graphene layers on the Ni surface and to obtain information about the quality and the number of layers deposited. Figure 6a shows Raman spectra taken at different locations on the synthesized films over $Si/SiO_2/Ni$ substrates by using an excitation wavelength of 532 nm, with a power density of 2.0 mW cm^{-2}. Strong peaks near 1580 cm^{-1} and 2690 cm^{-1} were found. Analysis of the frequencies and lineshapes of these peaks allows their assignment as the *G* and *G′* bands of graphene layers, respectively (Ferrari, Meyer et al. 2006). The peak located at 1345 cm^{-1} corresponds to the *D* band of graphitic carbon species, which is associated with the amount of defects in the crystalline structure of the graphene layers. The low cross section of the *D* band confirms that synthesized films are largely free of structural defects.

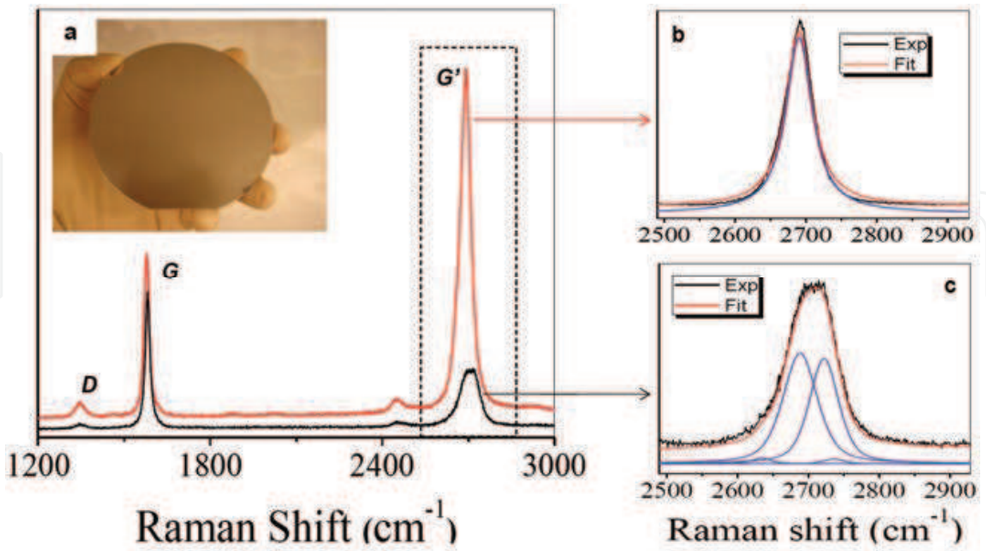

Fig. 6. (a) Raman spectrum obtained on as-synthesized graphene films on $Si/SiO_2/Ni$ substrates. *D*, *G* and *G′* Raman bands for graphene are labeled on each spectrum. (b) Raman spectrum obtained on a single layer graphene. (c) Raman spectrum of bilayer or few-layer graphene.

Interlayer interactions affect the Raman fingerprints for single-layer, bilayer, and few-layer graphene, allowing unambiguous identification of graphene layers. Figure 6b shows the Raman spectrum of single-layer graphene in the synthesized films. Single Lorentzian fit of the *G'* band is characteristic of monolayer graphene. On the other hand, a subtle splitting, up-shift of nearly 15 wavenumbers and broadening observed in the *G'* band that can be fit with four Lorentzian peaks, as shown in Figure 6c, which constitute the spectroscopic signature of bilayer graphene (Ferrari, Meyer et al. 2006; Gupta, Chen et al. 2006). The domain size for the single-layer, bilayer, and few-layer graphene is typically around 1-2 um, which is likely due to the grain size of the polycrystalline nickel film. Extensive Raman characterization over as-synthesized samples consistently showed the presence of graphene with less than five graphene layers (Cancado, Reina et al. 2008). No signature of multi-layer or bulk graphite was found in the films deposited

2.4 Graphene synthesis: Polycrystal vs single-crystal substrate

Polycrystalline Ni has been shown to be a good substrate for graphene synthesis by CVD, but the percentage of monolayer or bilayer graphene is limited by the grain size of crystalline Ni obtained by thermal annealing. We, among other groups, have reported the synthesis of wafer-scale few-layer graphene by CVD on the surface of polycrystalline Ni (Gomez, Zhang et al. 2009; Reina, Jia et al. 2009). Our results suggest that during the synthesis carbon atoms tend to segregate on nucleation sites on the Ni surface to form multiple-layer graphene grains. The formation of such multilayer domains is believed to be correlated to different factors including the abundance of defects and grain boundaries on the polycrystalline Ni substrate. It is therefore particularly interesting to investigate the formation of graphene on single crystal Ni due to the absence of interface boundaries. In addition, the (111) orientation is especially interesting due to the excellent lattice match between graphene/graphite and Ni (111) face, where the hexagonal lattice constant of 2.497 Å for Ni (111) provides an excellent match to that of 2.46 Å for graphite (see table 2) (Eizenberg and Blakely 1979).

The process of graphene growth on Ni can be divided into two parts: the first is carbon segregation from bulk Ni to Ni surface in an intermediate temperature range (~ 1065-1180 K), and the second is carbon precipitation which happens when the system temperature decreases (<1065 K). Carbon segregation and precipitation tend to happen at the grain boundaries (Shelton, Patil et al. 1974). This can be related to the fact that the impurities in transition metals tend to segregate at grain boundaries, which can be rationalized by considering that disorder and vacancies at such locations can readily act as active sites for the interaction and accumulation of impurities during cooling. In the specific case of carbon dissolved in nickel, this means that grain boundaries can be good nucleation sites for carbon segregation and hence, for multilayer graphene formation. Therefore, grain boundaries may play an important role in both the carbon segregation and precipitation processes during graphene synthesis.

Ni(111) intersticious distance (Å)	C-C bond length (Å)	Ni lattice constant (Å)	C lattice constant (Å)	Lattice constant mismatch (%)
1.412	1.420	2.517	2.4610	2.2

Table 2. Parameters correlating graphene and Ni (111).

Three different annealing rates on polycrystalline Ni were used. Temperature was increased from room temperature to 900°C at 3, 1 and 0,65 °C/s, for *fast, medium* and *slow* annealing rates, respectively. Annealing of Ni films was conducted in H_2 atmosphere. XRD spectra after the thermal annealing process are shown in Figure 7a. The first three spectra from top to bottom correspond to fast, medium and slow rate annealing on polycrystalline Ni, and the last one is collected from Ni (111) after annealing. All the spectra were normalized for the analysis. While all four samples show a strong peak corresponding to Ni (111), the polycrystalline Ni samples display an additional Ni (200) peak at 2θ = 52.16°, with intensity being highest for fast annealing and lowest for slow annealing. In contrast, the single crystalline Ni XRD spectrum shows no peak for Ni (200) (Figure 7b). Therefore, we can conclude that slower thermal annealing favors the formation of crystalline Ni (111) grains with less grain boundaries for polycrystalline Ni samples.

Graphene was synthesized by CVD at 900 °C at atmosphere pressure, and a cooling rate of 16 °C/min was used down to 500 °C. The details of the synthesis procedures are reported in the literature (Gomez, Zhang et al. 2009). Figure 7.c-j depicts the optical images of Ni substrates after graphene synthesis. Figure 7c and d, 7e and f, and 7g and h correspond to polycrystalline Ni samples obtained with fast, medium and slow thermal annealing rates, respectively. The darker regions are confirmed to consist of multilayer graphene (≥3 layers), while the lighter regions are confirmed to be monolayer/bilayer graphene.

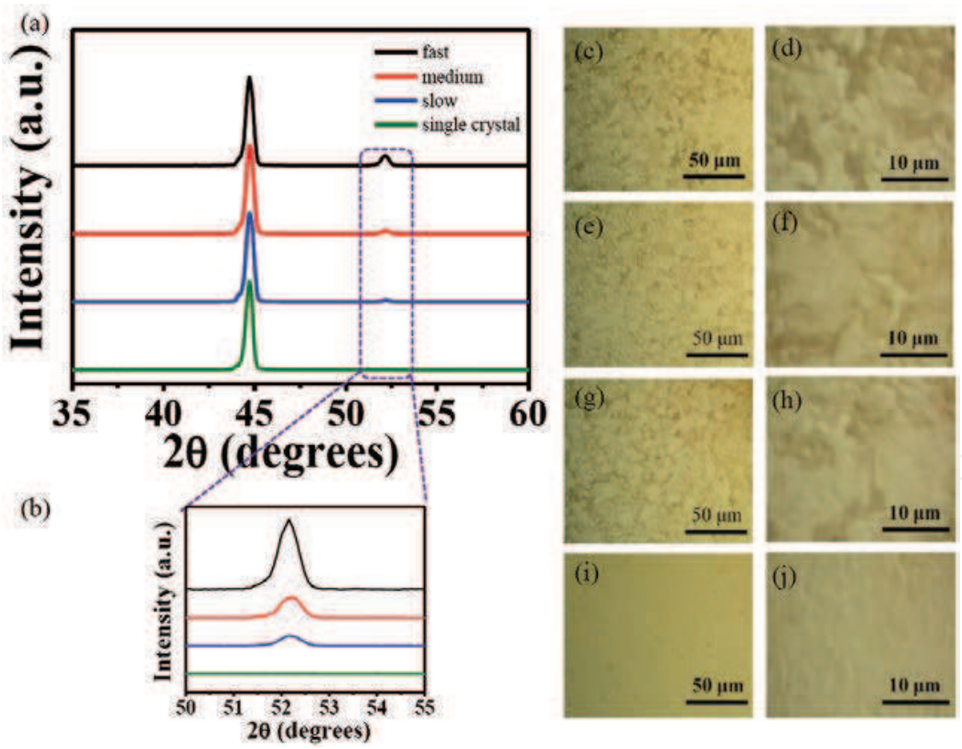

Fig. 7. (a) XRD spectra collected from polycrystalline Ni with fast (black), medium (red), and slow (blue) annealing rates and Ni (111) single crystal (green). (b) XRD spectra of peaks at 2θ = 52.16° (assigned as Ni (200)). (c-j) Micrographs of graphene CVD grown on polycrystalline Ni with fast (c, d), medium (e, f) and slow (g, h) annealing rates; and on Ni (111) (i, j).

Data shown on Figure 7c-h indicates that the percentage of multilayer graphene formation increases as the polycrystallinity of the Ni substrate increases; which suggests that the formation of multilayer graphene can be attributed to the increase of carbon segregation localized at polycrystalline grain boundaries, while the formation of monolayer/bilayer graphene is mainly obtained on the flat central areas of large crystalline grains. This is further confirmed on Figure 7i-j, where graphene grown on single crystal Ni (111) reveals scarce formation of multilayer graphene domains. The observation can be understood by considering the absence of inter-plane grain boundaries on the surface of Ni (111) and therefore a shortage of nucleation sites for multilayer graphene formation. Thus, mostly monolayer/bilayer graphene is uniformly formed on the surface of Ni (111) single crystal.
Based on the discussion above, a graphene growth mechanism is shown in Figure 8. Due to the high solubility of carbon in Ni, carbon first diffuses into bulk Ni, and then segregates and precipitates onto Ni surface. In the carbon/Ni (111) system, the surface roughness is negligible with almost no grain boundaries, which allows uniform segregation of carbon onto the Ni (111) surface, thus forming single layer graphene (Figure 8a and c). In contrast, in the carbon/ polycrystalline Ni system, the Ni surface is heavily populated by the grain boundaries, especially inter-plane grain boundaries, which allow the accumulation of carbon at these sites during the segregation phase and lead to the formation of multilayer graphene (Figure 8b and d). Therefore, multilayer graphene tends to form at the boundaries, while monolayer graphene tends to form on Ni (111) surface (Zhang, Gomez et al.). This growth mechanism differs significantly from that present on CVD graphene synthesized on Cu, where graphene is formed due to a self-limiting surface reaction instead of a segregation/precipitation process. (Li, Cai et al. 2009)

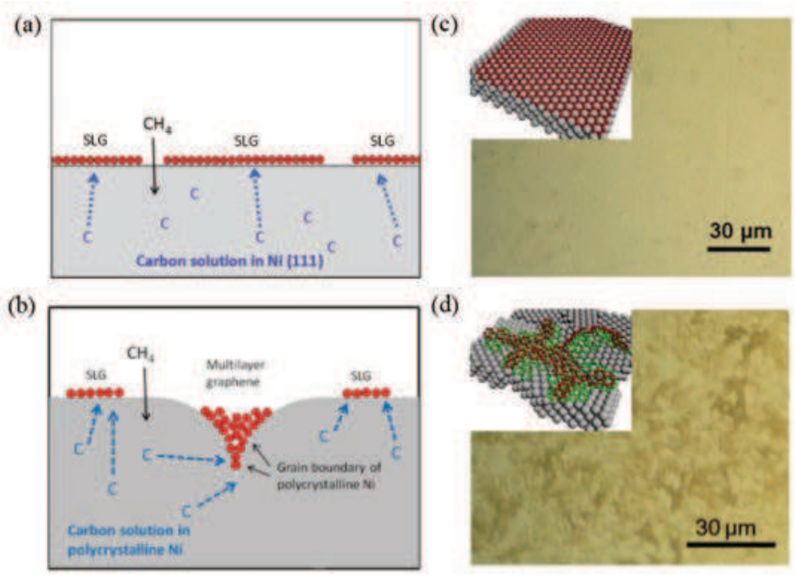

Fig. 8. (a-b). Schematic diagrams of graphene growth mechanism on Ni (111) (a) and polycrystalline Ni surface (b). (c). Optical image of graphene/ Ni (111) surface after the CVD process. The inset is a three dimensional schematic diagram of a single graphene layer on Ni (111) surface. (d). Optical image of graphene/polycrystalline Ni surface after the CVD process. The inset is a three dimensional schematic diagram of graphene layers on polycrystalline Ni surface. Multiple layers formed from the grain boundaries.

The formation of graphene layers on Ni surface was confirmed by micro-Raman spectroscopy after the CVD process. Figure 9a and b show ten typical spectra collected from different locations on the synthesized graphene films on Ni (111) and polycrystalline Ni, respectively. The low intensity of D band (~ 1350 cm^{-1}) confirms that the graphene formed on both Ni (111) and polycrystalline Ni surfaces are of low defects. Peaks located at ~ 1590 cm^{-1} and ~ 2700 cm^{-1} are assigned as G and G′ bands of the graphene layers, respectively.

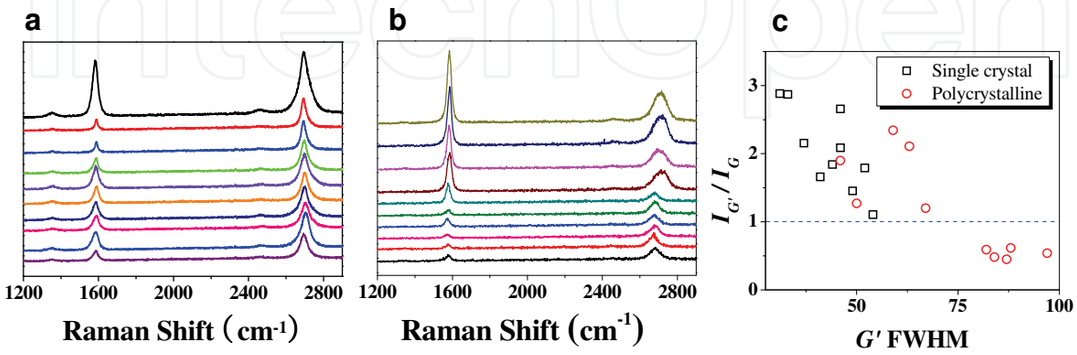

Fig. 9. (a,b) Raman spectra of graphene grown on Ni (111) and polycrystalline Ni, respectively. (c) ($I_{G'}/I_G$) v.s. G′ FWHM of graphene on Ni (111) and polycrystalline Ni.

All ten spectra collected from graphene on Ni (111) show single Lorentzian lineshape and narrow linewidth (25 – 55 cm^{-1}). Furthermore, they exhibit G′ to G peak intensity ratios ($I_{G'}/I_G$) larger than unity, typical for monolayer/bilayer graphene. In sharp contrast, upshifts and line broadening typical of multilayer graphene are seen on polycrystalline Ni. Figure 9c shows a plot of $I_{G'}/I_G$ values versus Full Width at Half Maximum (FWHM) of G′ bands. Graphene on single crystal Ni have $I_{G'}/I_G$ higher than unity with narrow FWHM, which corresponds to the spectroscopic signature of monolayer/bilayer graphene.

Further analysis includes the collection of about 800 Raman spectra over 3000 μm^2 area. The $I_{G'}/I_G$ values were then extracted from the spectra. Figures 10a,d show the $I_{G'}/I_G$ contour maps of graphene on Ni (111) and polycrystalline Ni, respectively. Nearly 92% of Raman spectra collected from the graphene on Ni (111) surface shows the hallmark of monolayer/bilayer graphene. In contrast, the percentage of monolayer/bilayer graphene was only close to 73% from the graphene film grown on polycrystalline Ni. Optical contrast of graphene atop Si/SiO_2 substrates, with 300 nm oxide thickness, further confirms that films transferred from Ni (111) and poly Ni consisted of monolayer/bilayer and multilayer graphene, respectively (Figure 10 c, f).

In summary, these findings demonstrate that the CVD synthesis of graphene on the (111) face of single crystal Ni favors the formation of highly uniform monolayer/bilayer graphene on the Ni surface, and simultaneously hinders the formation of multilayer graphene domains. Our results are understood on the basis of the diffusion-segregation model for carbon precipitation on Ni surface (Shelton, Patil et al. 1974), where the uniform and grain-boundary-free surface of Ni (111) single crystal provides a smooth surface for uniform graphene formation. In contrast, the rough surface of polycrystalline Ni with abundant grain boundaries facilitates the formation of multilayer graphene. Graphene produced over

Si/SiO_2 wafers can be very useful for device fabrication, and our approach may serve as the foundation for the growth of single-domain graphene over macro-scale areas such as complete wafers.

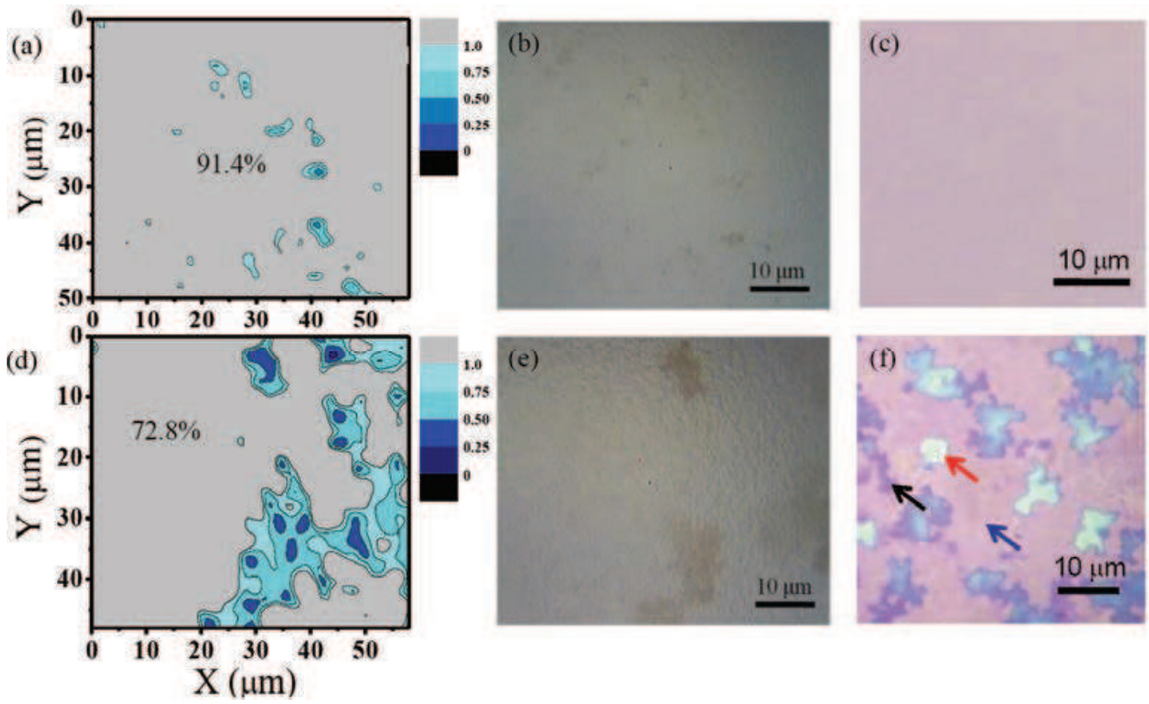

Fig. 10. Micro Raman maps of I_G/I_G of about 800 spectra collected over 3000 μm² area on as-grown graphene atop Ni (111) (a) and polycrystalline Ni (d) surfaces. Micrographs of the areas analyzed on Ni (111) (b) and polycrystalline Ni (e). Optical image of graphene grown on Ni (111) (c) and polycrystalline Ni (f) after transferred onto $Si.SiO_2$ substrates.

3. Applications of large scale graphene

Graphene outstanding electrical and thermal conductivities make it an exciting material with high potential to replace silicon and surpass its performance in the next generation of semiconductors devices. Applications of graphene films are strongly linked to its electronic structure. The energy dispersion of graphene is given by:

$$E_{g2D}(k_x, k_y) = \pm t\left[1 + 4cos\left(\frac{\sqrt{3}k_x a}{2}\right)\cos\left(\frac{k_y a}{2}\right) + 4cos^2\left(\frac{k_y a}{2}\right)\right]^{1/2} \quad (1)$$

The positive part of the energy dispersion describes the π* anti-bonding energy band and the negative part is the π bonding energy band. Interestingly, the π* anti-bonding and π bonding bands are degenerate at the *K* points through which the Fermi energy passes.
The first significant feature of this result is that, since the energy band is exactly symmetric about the point $E = E_{2p} = 0$, and this condition is met only at Dirac point. It follows that for exactly half filling of the band the density of states at the Fermi level is exactly zero and undoped graphene is a perfect semimetal. At zero doping, the lower half of the band is filled exactly up to the Dirac Point. If by applying a suitable "gate" voltage to the graphene

relative to the substrate we induce a nonzero charge, this is equivalent to injecting a number of electrons in the upper half or holes in the lower half of the Dirac cones. This effect is known as the field effect (Figure 11).

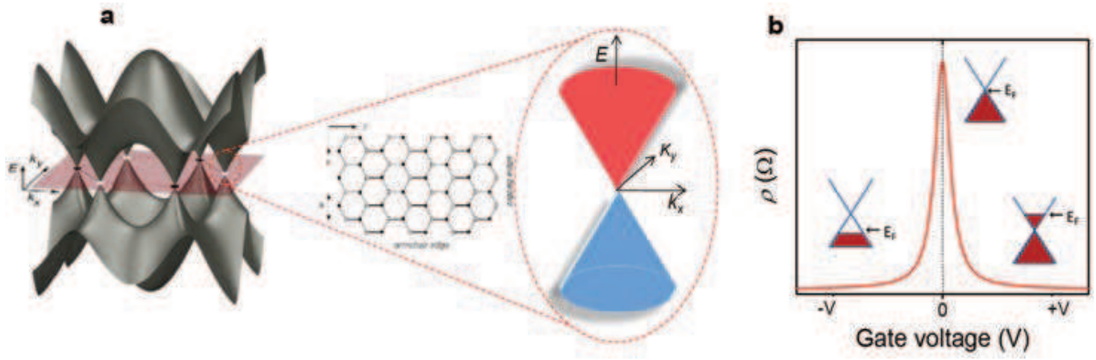

Fig. 11. (a) Energy dispersion relations of graphene. Inset shows the energy dispersion relations along the high symmetry axes near the Dirac point. (b) Conical low-energy spectrum $E(k)$, indicating changes in the position of the Fermi energy E_F with changing gate voltage V_g. Positive (negative) V_g induce electrons (holes) in concentrations $n =$ V_g where the coefficient 7.2 10^{10} cm^{-2} V^{-1} for field-effect devices with a 300 nm SiO_2 layer used as a dielectric.

3.1 Graphene for nanoelectronics

Graphene exhibits a pronounced ambipolar electric field effect such that charge carriers can be tuned continuously between electrons to holes. Single layer graphene atop a thermally grown SiO_2 layer on a highly doped Si substrate may serve as a prototype of a field effect transistor. Under this configuration SiO_2 serves as an insulating layer, so a back-gate voltage can be applied to vary carrier concentration (figure 11b). Early graphene FET devices demonstrated by Novoselov exhibited dopant concentrations as high as 10^{13} cm^{-2} and achieved a mobility that could exceed 10,000 cm^2 /Vs (Novoselov, Geim et al. 2004). This translates into ballistic transport on submicron scales. The room-temperature mobility is limited by impurities or corrugations of the graphene surface, which means that it can still be improved significantly up to the order of 10^5 cm^2 /Vs (Bolotin, Sikes et al. 2008; Du, Skachko et al. 2008).

Electrons in graphene behave like massless relativistic particles, which govern most of its electronic properties. One of the most important consequences of such unusual dispersion relation is the observation of half-integer Quantum Hall Effect and the absence of localization, which can be very important for graphene-based field effect transistors (Geim and Novoselov 2007). Mechanical exfoliation of highly ordered pyrolitic graphite (HOPG) or high purity graphite flakes can lead to obtain graphene crystals with very few defects, which in turn exhibit high mobility of the charge carriers. Figure 12 shows scanning electron microscopy (SEM) and atomic force microscopy (AFM) of the graphene-based device reported in the literature as having the highest electron mobility to date (Bolotin, Sikes et al. 2008). The graphene film was obtained by mechanical exfoliation of graphite on Si/SiO_2 substrate in which the oxide layer underneath the graphene was etched in order to obtain a free-standing graphene flake connecting the metal electrodes.

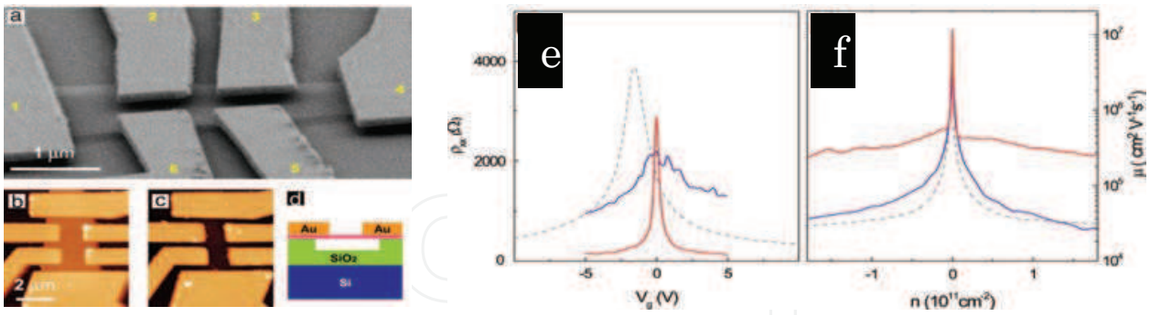

Fig. 12. (a) SEM image of a typical suspended six-probe graphene device. AFM image of the suspended device before (b) and after (c) the measurements and graphene removal oxygen plasma etch. (d) Device schematic, side view, suspended single-layer graphene is colored pink. (e) Measured four-probe resistivity as a function of gate voltage before (blue) and after (red) current annealing. Data from traditional high-mobility device on the substrate is plotted with gray dotted line. (f) Mobility μ = as a function of carrier density n for the same devices.

Electrical measurements of resistivity vs. gate voltage show the intrinsic ambipolar behavior of graphene. It was also established that the transfer characteristics of the device is greatly improved after undergoing a high-current annealing process to remove contaminants from the graphene surface. The mobility μ for this device reaches the outstanding value of 230,000 cm²/Vs measured at the highest carrier density n = 2x10^{11} cm^{-2}. Such high mobility would in principle favor high frequency performance. Furthermore, graphene devices pursuing high frequency have demonstrated encouraging characteristics, exhibiting a cutoff frequency f_T of 26 GHz, which is the frequency at which the current gain becomes unity and signifies the highest frequency at which signals are propagated (Lin, Jenkins et al. 2008). Only recently, P. Avouris and collaborators reported the fabrication of graphene FETs on SiC substrates with cutoff frequency of 100 GHz for a device of gate length of 240 nm and using a source-drain voltage of 2.5 V (Lin, Dimitrakopoulos et al.). This f_T exceeds those previously reported for graphene FETs as well as those for Si metal-oxide semiconductor FETs for the same gate length (~40 GHz at 240 nm) (Meric, Baklitskaya et al. 2008; Moon, Curtis et al. 2009).

3.1.1 CVD graphene device fabrication

Despite the advance in graphene based nanoelectronic devices shown above, it is worth noting that the methods employed to obtain graphene on most works are not scalable. In this section, we present our approach to scalable graphene and demonstrate graphene FETs to illustrate potential applications of CVD graphene for nanoelectronics.

Two methods were used to transfer the as-synthesized graphene film to target substrates. The first approach consisted of immersing the graphene-on-nickel sample into a nickel etchant solution. This process removed nickel and left graphene films deposited on the underlying Si/SiO_2 substrate. Graphene transfer from the original Ni substrate to a Si/SiO_2 substrate allowed the fabrication of back-gated FETs at large scale (Figure 13a).

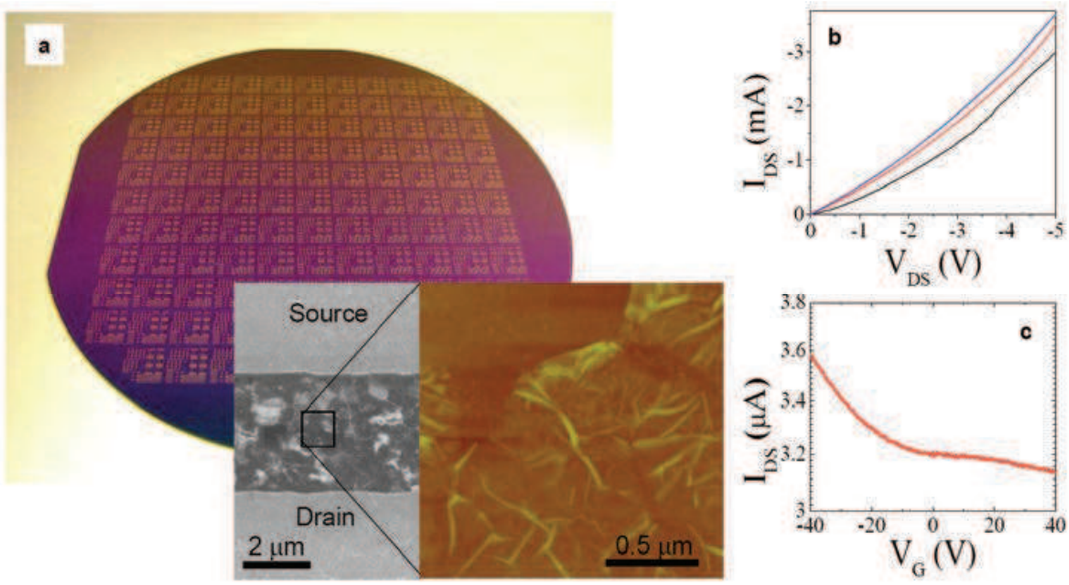

Fig. 13. (a) 4-inch wafer with back-gated few-layer graphene devices; insets show SEM and AFM images of a typical device and device channel, respectively. (b) I_{DS}-V_{DS} measurements for different gate voltages, V_G = 2.5 V, 1.5 V and -1.5 V for the black, red and blue curves, respectively and (c) I_{DS}-V_G curve of one of the FET devices for V_{DS} = 0.01 V.

Four-probe measurements performed on the FLG films revealed a sheet resistance of ~68 kΩ/sq. I_{DS}-V_{DS} characteristics depicted in figure 13b shows that the drain current increases with the increase of negative gate voltage, indicating a weak p-type behavior in the films. Figure 13c shows the transfer characteristics for a device with channel width of 20 μm and channel length of 4 μm. Most devices were highly conductive and exhibited a weak modulation of the drain current by the gate bias, which is consistent with a 2D semimetal.

Compared to carbon nanotubes, graphene FETs typically exhibit low current on/off ratios, which can be improved significantly by patterning graphene into nanoribbons (Han, Ouml et al. 2007). Single graphene layer is a zero-gap semiconductor, but interlayer interactions bring in a semimetal behavior in FLG. Therefore, the transfer characteristics observed in Figure 2.5c can be attributed to a screened gating effect due to irregularities of the film and the presence of more than two graphene layers in the films. A striking difference is observed in the transfer characteristics of graphene FETs with single or bilayer graphene as the device channel, as can be observed in Figure 14 where typically 3-4 inch diameter CVD graphene wwere transferred to Si/SiO_2 wafers for graphene FET fabrication at wafer scale. Figure 14 shows representative I-Vg characteristics of single and bilayer graphene FTEs synthesized on Cu and Ni substrates. The nearly-symmetric ambipolar transfer characteristics exhibited by these devices are typical from single or bilayer graphene FETs with high quality and low doping concentration. Graphene FETs offer the advantage of gate voltage dependent hole or electron conduction.

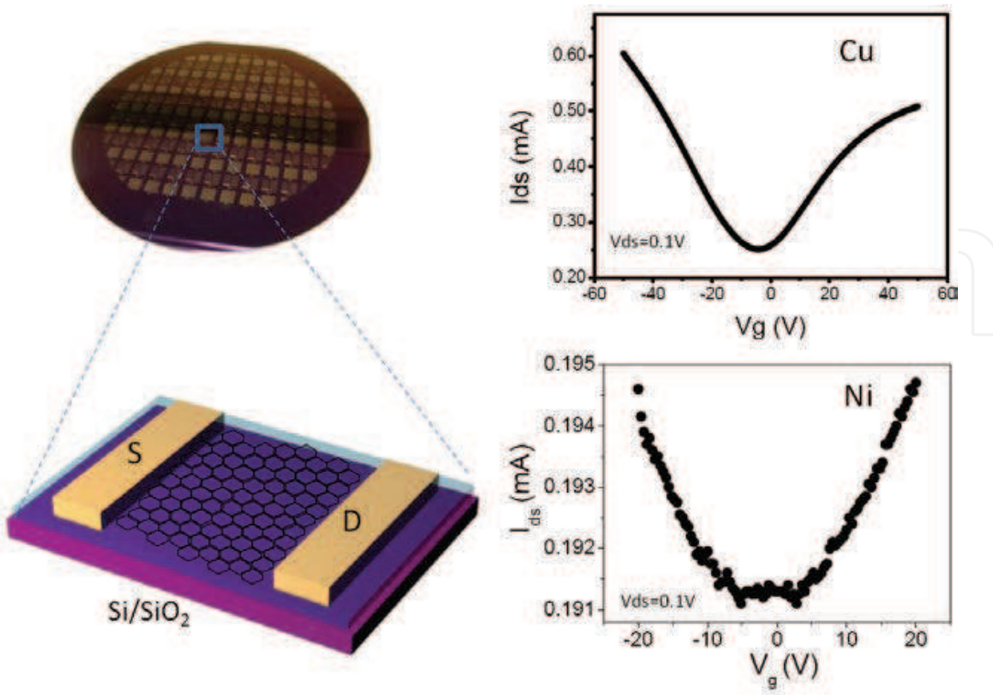

Fig. 14. Left: Photograph of CVD graphene FETs fabricated at large scale on a 4-inch Si/SiO_2 wafer and schematic of the graphene FET device structure. Right: IV_g characteristics of CVD graphene FETs synthesized on copper (up) and nickel (down).

3.2 CVD graphene for macroelectronics: Transparent conductive films

Another intrinsic property of graphene is its transparency. A single sheet of graphene absorbs only 2.3 % of the incident light. Such combination of high conductivity and low light absorption makes this material an ideal candidate as a transparent conductive film. It is very tempting to use the unique properties of graphene for technology applications even beyond graphene FET applications. Composite materials, photodetectors, support for biological samples in TEM, mode-lockers for ultrafast lasers and many more areas would gain strongly from using graphene for non-FET purposes.

3.2.1 Large scale transfer of graphene

Graphene obtained by chemical vapor deposition can be readily transferred to a number of different substrate surfaces at large scales. We have developed a transfer technique that allows transfer with 100% efficiency at large scales (Gomez De Arco, Zhang et al.; Gomez, Zhang et al. 2009). This technique employs a thin layer of poly-methylmethacrylate (PMMA) which is deposited on top of the as-synthesized graphene on $Si/SiO_2/Ni$ substrates. Dissolution of the metallic substrate where graphene is synthesized yields a free-standing PMMA/graphene stack, which then can be transferred by direct graphene contact onto any substrate, including transparent substrates such as glass and polyethylene terephthalate (PET) sheets. Figure 15a shows a schematic representation of the graphene transfer process to transparent substrates, either rigid or flexible. This large-scale transfer method is reliable and fully compatible with semiconductor industry procedures and technologies.

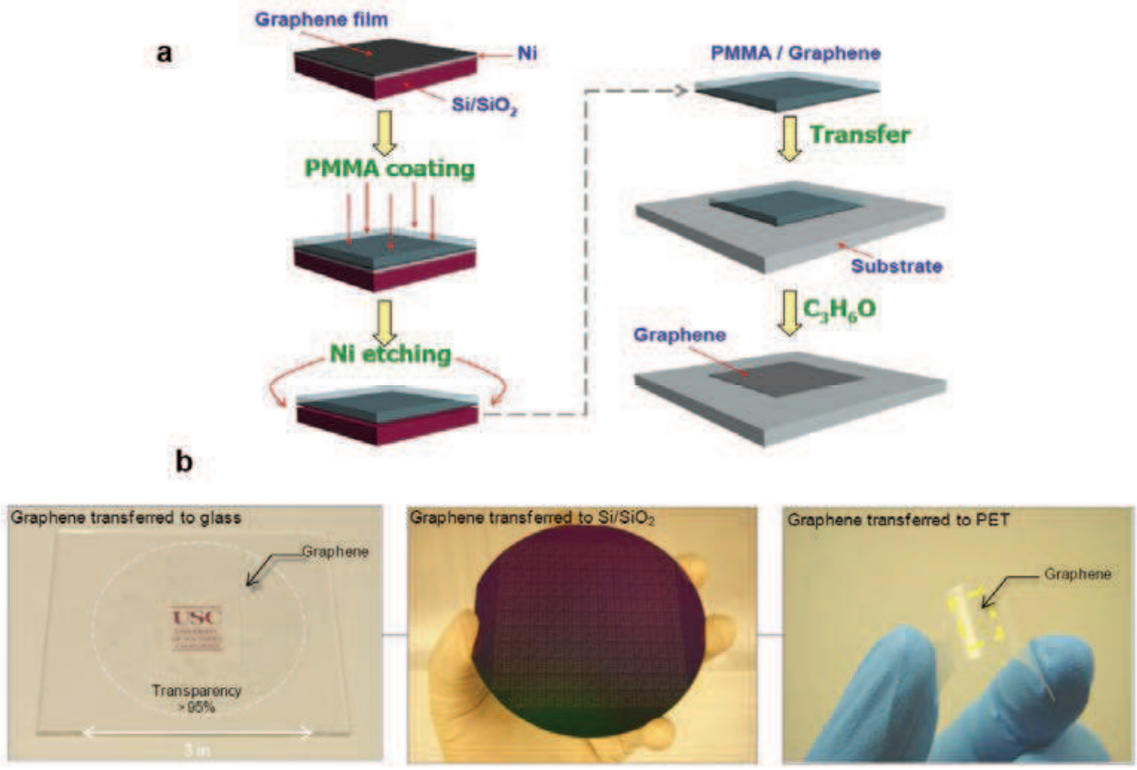

Fig. 15. (a) Schematic of the CVD graphene transfer process onto transparent substrates. (b) 3-4 inch diameter graphene film transferred to glass, Si/SiO2 and PET.

Light transmission spectra taken on different locations of the 10cm diameter transferred area of the glass substrate yielded a percent of transmittance higher than 96%, which is consistent with the presence of maximum 2 layer of graphene over the large transferred area. Graphene transfer to flexible polyethylene terephthalate (PET) substrates, as shown in figure 11b, opens exciting possibilities of large scale graphene in flexible, transparent electronics. The graphene transferred to flexible PET substrates is highly flexible and highly conductive, with sheet resistance of < 250 Ohm/sq.

3.2.2 Graphene applications in photovoltaics

3.2.2.1 Photovoltaic cells: Graphene vs ITO

Solar energy harvesting using organic photovoltaic (OPV) cells has been proposed as a means to achieve low-cost energy due to their ease of manufacture, light weight and compatibility with flexible substrates. A critical aspect of this type of optoelectronic device is the transparent conductive electrode through which light couples into the device. Conventional OPVs typically use transparent indium tin oxide (ITO) or fluorine doped tin oxide (FTO) as such electrodes (Peumans, Yakimov et al. 2003). However, the scarcity of indium reserves, intensive processing requirements, and highly brittle nature of metal oxides impose serious limitations on the use of these materials for applications where cost, physical conformation, and mechanical flexibility are important.

Graphene monolayer has a transparency of 97-98 percent and the sheet resistance of undoped graphene is of the order of ~6kΩ; for which graphene films are suitable for applications as transparent conductive electrodes where low sheet resistance and high optical transparency are essential (Gomez De Arco, Zhang et al.). Conventional methods to obtain graphene thin films such as epitaxial growth, micromechanical exfoliation of graphite and exfoliation of chemically oxidized graphite are either expensive, unscalable or yield graphene with limited conductivity due to a high defect density. However, chemical vapor deposition has surged as an important method to obtain high quality graphene films. In particular, films with sheet resistance of 280 Ω/sq (80% transparent) and 770 Ω/sq (90% transparent) have been reported in the literature for graphene synthesized on Ni films, while sheet resistance of 350 Ω/sq (90% transparent) has been reported for CVD graphene on Cu films, which represents a good advance in the use of graphene as transparent conductive films. Another advantage of CVD is its scalability; we have reported wafer-scale synthesis and transfer of single- and few-layer graphene for transistor and photovoltaic device fabrication (Gomez De Arco, Zhang et al.; Gomez, Zhang et al. 2009)[25].

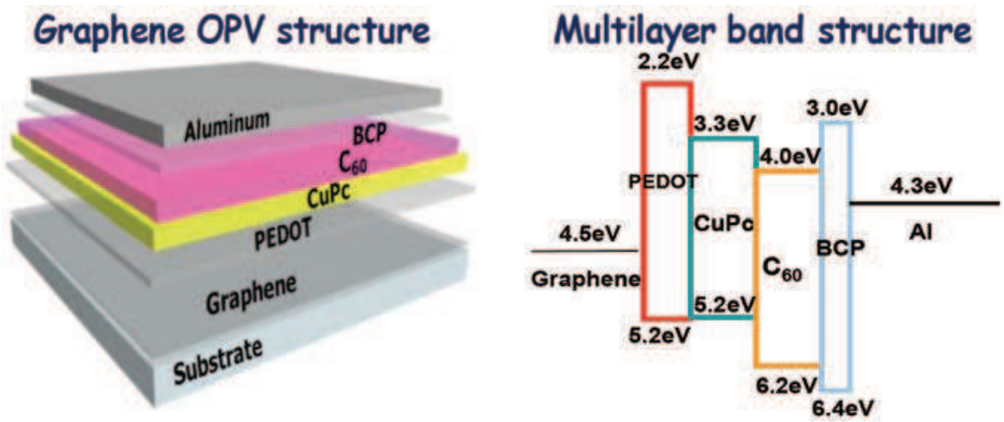

Fig. 16. Schematic representation of the energy level alignment (right) and construction of the heterojunction organic solar cell fabricated with graphene as anodic electrode: CVD graphene / PEDOT / CuPc / C_{60} / BCP / Al.

Graphene electrodes were fabricated by transferring as-grown CVD graphene films onto pre-cleaned PET substrates. Both substrates were solvent cleaned and passivated by spin coating a thin layer of poly(3,4-ethylenedioxythiophene)-poly(styrenesulfonate) (PEDOT:PSS). Organic thin films and the aluminum cathode were consecutively deposited by thermal evaporation to form a multilayered configuration: CVD graphene or ITO / PEDOT:PSS / Copper phthalocyanine (CuPc) / Fullerene (C_{60}) / Bathocuproine (BCP) / Aluminum (Al). Aluminum cathodes were deposited through a shadow mask with circular openings of 0.75 mm^2. Figure 16 shows a representation of the OPV cell and the band structure of the stacked materials.

Use of the PEDOT:PSS coating as the electron blocking layer decreased the conductivity of the PEDOT:PSS/CVD Graphene film to 2.1 kΩ/sq, while for the PEDOT/ITO film it remained ~1 kΩ/sq. PEDOT:PSS was expected to help mitigate the brittle nature of the ITO electrode to enhance its performance under bending conditions, and interestingly, PEDOT:PSS passivation of ITO was also found to improve the rectification behavior of the devices.

Optical excitation of the CuPc (C_{60}) leads to the donation of an electron (hole) to C_{60} (CuPc) and the photogenerated charge carriers are swept to the external contacts producing a measurable light-generated current. Current density vs. voltage or $J(V)$ characteristics were measured in air at room temperature in the dark and under spectral mismatch corrected 100 mW/cm² white light illumination from an AM 1.5G filtered 300 W Xenon arc lamp. Routine spectral mismatch correction was used to reduce measurement errors. Chopped monochromatic light (250 Hz, 10 nm FWHM) and lock-in detection was used to perform all spectral responsivity and spectral mismatch correction measurements.

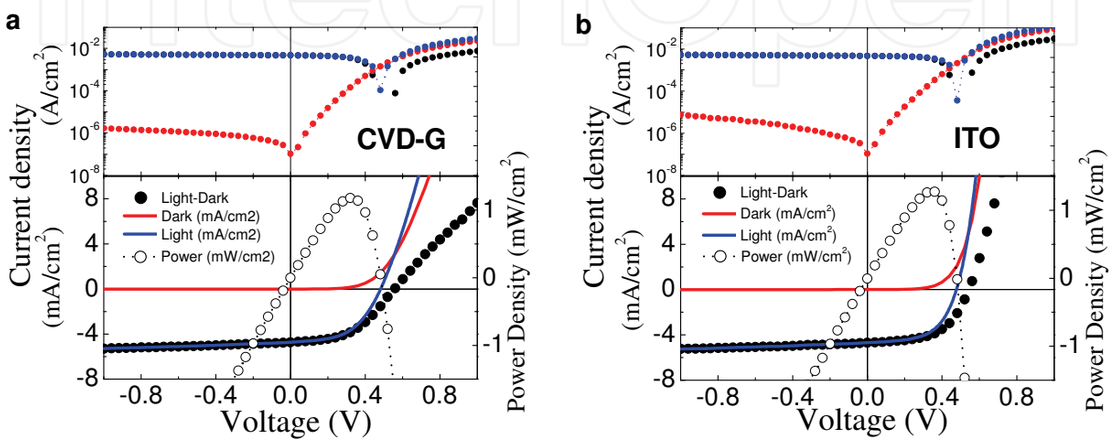

Fig. 17. Logarithmic (up) and linear (down) current density and power density vs voltage characteristics of CVD graphene (a) and ITO (b) OPV cells on PET under dark (red traces) and 100 mW/cm² AM1.5G spectral illumination (blue traces). The light-dark current difference and output power density of the cells is plotted on (a) and (b) as filled and open circle traces, respectively.

We compared the $J(V)$ characteristics of a typical photovoltaic cell obtained with CVD graphene (R_{sheet}: 3.5 kΩ/sq, T: 89%) against a typical cell obtained with an ITO anode (R_{Sheet}: 25 Ω/sq, T: 96%), that were fabricated under identical experimental conditions. Figure 17a and 17b show semi-log (up) and linear (down) $J(V)$ plots obtained from CVD graphene and ITO OPV cells, respectively. Red and blue traces correspond to the current density measured in the dark and under illumination, respectively. The output power density of the cells (P), which is given by $P = J \cdot V$, is shown in Figure 17 as open circle traces for which the maximum point on the curve corresponds to the maximum output power density (P_{max}) of the device.

For an incident power density, P_{inc} = 100 mW/cm², the power conversion efficiency ($\eta = P_{max}/P_{inc}$) and other performance parameters such as the short circuit current density (J_{sc}), open circuit voltage (V_{oc}), and fill factor (FF) are summarized in Table 3. It is clearly observed from the semi-log plots in Figure 17 that both devices have nearly identical V_{oc} under illumination conditions, which suggests similar recombination behavior in both cells. Moreover, unlike OPVs reported for reduced GO anodes which presented large leakage (Wu, Becerril et al. 2008; Tung, Chen et al. 2009), there is no noticeable current density leakage from any of the CVD graphene OPV cells.

The $J(V)$ characteristics of the CVD graphene cell and ITO control devices were highly similar. Analysis of figure 17 reveals that despite the lower transparency and higher R_{Sheet} of the CVD graphene electrode, CVD graphene solar cell exhibits an output power density

nearly 93% of that shown by the ITO device. We also observed that CVD graphene OPV cells were more sensitive to the anode conductivity, and hence, to its capacity to pull holes from the active layers than to its transparency.

Results above can be rationalized by considering that the sheet resistance increases to similar values on both electrodes after being coated with PEDOT:PSS. In this escenario, charge injection from the active layers of the OPV cells may be limited by the PEDOT:PSS layer, thus yielding similar performance on both cells. We fabricated OPV cells on PET/PEDOT:PSS substrates without graphene or ITO and all of them produced open circuit characteristics. Although PEDOT:PSS was used on both, graphene and ITO OPV cells, the performance of the cells was measured by puncturing the PEDOT:PSS layer to contact the underlying electrode material, which confirms that CVD graphene and ITO anodes, instead of PEDOT:PSS are the ultimate electrodes in the hole extraction process of the devices.

Anode	**J_{sc} (mA/cm2)**	**V_{oc} (V)**	**FF**	**η**
CVD graphene	4.73	0.48	0.52	1.18
ITO	4.69	0.48	0.57	1.27

Table 3. Performance details of OPV cells built on PET.

To estimate the impact of resistive losses on device performance the $J(V)$ dependence under illumination was modeled according to a modified form of the Shockley equation, which is commonly applied to describe the current density (J) vs. voltage (V) characteristics of organic solar cells, given by:

$$J = J_s\left\{\exp\left(\frac{V - JR_s}{nV_t}\right) - 1\right\} + \frac{V - JR_s}{R_p} - J_{ph} \tag{2}$$

where R_s, R_p, J_s, J_{ph}, n, and V_t are the lumped series resistance, lumped parallel resistance, reverse-bias saturation current-density, photocurrent-density, diode ideality factor, and thermal voltage respectively for a single diode circuit model. As a practical matter, the transcendental nature of Eq. 2 was resolved by expressing it in terms of the Lambert-W function(Hayes 2005) (see supporting information) to give:

$$J = \frac{nV_t}{R_s}W_0\left\{\frac{J_s R_s R_p}{nV_t(R_s + R_p)}\exp\left(\frac{R_p}{nV_t}\frac{V + R_s(J_{ph} + J_s)}{(R_s + R_p)}\right)\right\} - \frac{R_p(J_{ph} + J_s) - V}{(R_s + R_p)} \tag{3}$$

Where W_0 represents Lambert's function of the form $W(x)e^{W(x)}=x(V)$ (Ortiz-Conde, García Sánchez et al. 2000; Hayes 2005), which expresses the measured current-density dependence on applied voltage in terms of the model parameters for a single diode equivalent circuit model.

The modeled $J(V)$ and output power density obtained according to Eq. 3, are plotted as solid lines for the CVD graphene and ITO cells depicted in Figures 17a and 17b, respectively. The modeled data are compared against the experimentally measured values, plotted as open symbols in Figure 18, demonstrating that these CVD graphene based devices may be described by the generalized Shockley equation in the same way that their ITO based counterparts are commonly discussed. Modeling the data in this way allows us to estimate to what extent series resistive losses, parallel conductance, and recombination processes may impact device performance.

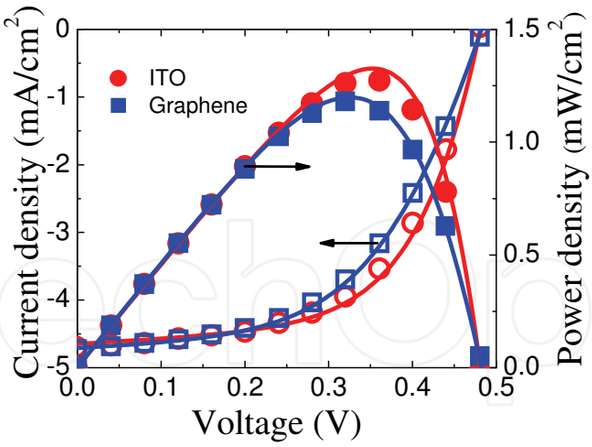

Fig. 18. Comparison of the modeled (solid lines) current density and power density curves of the graphene and ITO devices obtained from the Shockley equation against the experimentally (dots) obtained values.

The model ideality factors, parallel resistances and saturation current-densities were all comparable for the ITO and CVD graphene devices under illumination, having values of n = 2.4 and 2.6, R_p =1.47 kΩcm² and 1.62 kΩcm², and J_s =2.0 μA/cm² and 3.1 μA/cm², respectively, suggesting that the recombination and leakage processes are similar for both devices. The model series resistance calculated from Eq. 3 for the CVD graphene device is 12.6 Ωcm², which is less than 5 times that of the ITO device with R_s = 2.6 Ωcm², while the model photocurrent density (J_{ph}) for the CVD graphene device (4.75 mA/cm²) is higher than J_{ph} for the ITO device (4.66 mA/cm²). This indicates that the power output of the graphene based device is primarily limited by charge transport losses rather than optical transmittance losses. This constitutes a very promising result for CVD graphene transparent electrodes, which perform comparably to ITO, despite carrying a relatively higher sheet resistance.

3.2.2.2 Flexible photovoltaics: Graphene vs ITO

Given the good performance of OPVs with graphene electrodes, the question remains if such devices will perform well under strain-stress conditions. Current-voltage characteristics under bending of CVD graphene and ITO solar cells are shown in Figures 19a and b, respectively. We observed that the performance of both devices was slightly degraded upon bending. For instance, solar cells using CVD graphene electrodes withstood bending angles (curvature radii, surface strain) up to 138° (4.1 mm, 2.4%) while exhibiting good solar cell performance. In sharp contrast, ITO cells only withstood bending to 36° (15.9 mm, 0.8%) while showing poor performance, and failed completely to become an open circuit after being bent to 60° (9.5 mm, 1%). It is important to note that, with increased bending angle, the current density dropped for CVD graphene and ITO devices, while their open circuit voltage remained virtually unchanged. In some cases this effect can be associated with decreased illumination of the devices during bending. However, as both cells are subjected to similar bending conditions, the marked difference exhibited in the conversion efficiency between them cannot be attributed to irregular illumination induced by bending, but may be related to the presence of micro cracks on the ITO device.
To further investigate this, we plotted the fill factor vs. the bending angle of the OPV cells with CVD graphene and ITO electrodes (Figure 4.12a). The fill factor ($FF=P_{max}/J_{sc}V_{oc}$)

depends strongly on the output power of the cell, and is directly related to the cell conversion efficiency (η) by

$$\eta = FF \frac{J_{sc} V_{oc}}{P_{inc}} \times 100 \tag{4}$$

Gradual degradation of the initial fill factor, and hence, the conversion efficiency was observed on the CVD graphene cell as the bending angle increased; in contrast, the fill factor of the ITO device rapidly decayed to zero when bent at around 60°. Furthermore, we performed SEM measurements to investigate changes in film morphology that may have been introduced by bending of the devices. Figure 4.12b shows the appearance of micro-cracks throughout the ITO device, while no signs of micro-cracks or fissures were observed on the graphene device. Development of micro-cracks generated by mechanical stress in ITO, even at small bending angles, can substantially increase the film resistance, which has a key impact in reducing the fill factor. This agrees well with the observed decrease in output current density and power conversion efficiency of the solar cells without observing appreciable change in the V_{oc}. CVD graphene, being of organic nature and more flexible, surpasses the performance of ITO, which may easily crack under slight bending albeit PEDOT:PSS passivation. Therefore, the brittle nature of ITO plays a major role in the resulting poor performance of ITO-flexible organic solar cells, while the CVD graphene thin films exhibited good performance as flexible transparent electrodes (Gomez De Arco, Zhang et al.).

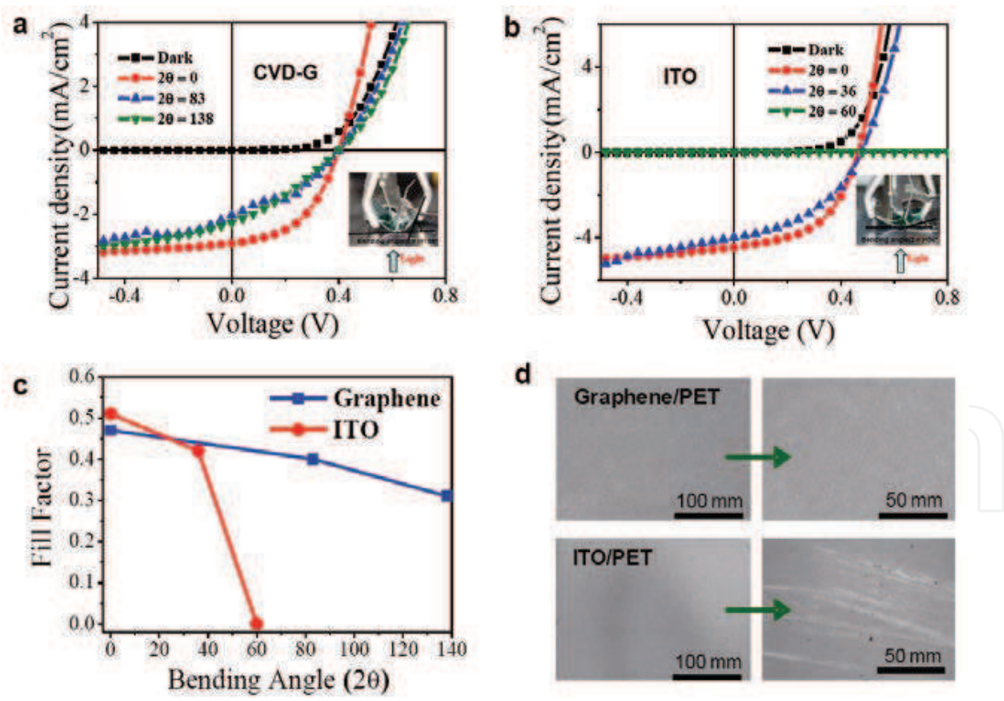

Fig. 19. Current density vs voltage characteristics of CVD-G **(a)** or ITO **(b)** photovoltaic cells under 100 mW/cm² AM1.5 spectral illumination for different bending angles. Insets show the experimental set up employed in the experiments. **c,** Fill factor dependence of the bending angle for CVD-G and ITO devices. **d,** SEM images showing the surface structure of CVD-G (up) and ITO (down) photovoltaic cells after being subjected to the bending angles described in **a** and **b.**

3.2.2.3 CVD graphene photovoltaic cells on rigid substrates

In order to explore the performance of graphene OPVs on rigid substrates, we fabricated solar cells on CVD graphene films transferred on glass (R_{Sheet}: 1.2 kΩ/sq, *T*: 82% at 550 nm) and glass substrates coated with ITO (Thickness: 150 nm, R_{Sheet}: 20 Ω/sq, *T*: 84% at 550 nm). *J(V)* characteristics of the fabricated devices are summarized on table 4.
Comparison of these devices shows that even though conversion efficiency of the CVD graphene device is lower, the overall performance of the CVD graphene photovoltaic cell is competitive, with *FF* comparable to that of the control ITO device. Higher transparency of the ITO film may lead to a higher exciton generation rate, which in turn is reflected in higher J_{sc} values. However, smoothness and thickness of the graphene film may favor charge injection and transport. The disparate power conversion efficiency observed between the two cells can be attributed to the higher sheet resistance and lower transparency of the graphene electrode in the G-OPV.

Anode	J_{sc} (mA/cm2)	V_{oc} (V)	FF	η (%)
CVD graphene	3.45	0.47	0.47	0.75
ITO	5.41	0.47	0.54	1.39
Red. GO (Wu et al.)	2.10	0.48	0.34	0.40
Red. GO (Wang et al.)	1.00	0.70	0.36	0.26

Table 4. Performance parameters measured CVD graphene and ITO photovoltaic cells built on glass as compared to GO OPV cells on glass reported in the literature.

Results shown here demonstrate CVD graphene as a feasible, scalable and effective material for highly transparent, continuous and flexible electrodes for OPVs (Gomez De Arco, Zhang et al.). This approach constitutes a significant advance towards the production of transparent conductive electrodes in solar cells. CVD graphene meets the most important criteria of abundance, low cost, conductivity, stability, electrode/organic film compatibility and flexibility that are necessary to replace ITO in organic photovoltaics, which may have important implications for future organic optoelectronic devices.

4. Conclusion

This chapter presented a chemical vapor deposition approach to solve some of the fundamental problems that hinder the realization of two-dimensional carbon nanostructure *graphene* as a viable technology in next generation electronic devices. This effort presented the development and implementation of a scalable method to produce high quality graphene at large scale. First, we presented a general introduction to 2 dimensional carbon nanomaterials followed by a more focused discussion on the structure and properties of graphene. Then we illustrated the development of a simple, scalable, and cost-efficient method to prepare graphene using methane-based CVD, with which we achieved high quality graphene synthesis at large scale. The presentation of this finding was complemented with the development of further work towards the synthesis of graphene on single crystal nickel, which demonstrated a strong influence of the substrate atomic arrangement, lattice order and surface smoothness on the thickness of the synthesized graphene. Single crystal Ni favored the formation of single and bilayer graphene over few-layer films. In addition, we presented graphene applications in nanoelectronics where we showed early FET devices with characteristic ambipolar behavior under gate bias for single and bilayer CVD graphene devices. CVD graphene applications in macroelectronics were

approached via its use as a transparent conducting film and as the transparent electrode in flexible organic photovoltaic cells. CVD graphene solar cells demonstrated outstanding capability to operate under bending conditions, outperforming largely ITO-based cells which displayed cracks and irreversible failure under bending. In general, CVD graphene shows great potential as a mass production transparent conductive film for applications in rigid and flexible electronics at the nano and macro scales.

5. Acknowledgment

The authors want to acknowledge support to the findings framed on this work from the National Science Foundation under Grant CCF-0702204. Authors also gratefully acknowledge Prof. M. Thompson and Prof. S. Cronin for kindly providing facilities and fruitful discussions.

6. References

Arenz, M., K. J. J. Mayrhofer, et al. (2005). "The effect of the particle size on the kinetics of CO electrooxidation on high surface area Pt catalysts." Journal of the American Chemical Society 127(18): 6819-6829.

Bolotin, K. I., K. J. Sikes, et al. (2008). "Ultrahigh electron mobility in suspended graphene." Solid State Communications 146(9-10): 351-355.

Cancado, L. G., A. Reina, et al. (2008). "Geometrical approach for the study of G ' band in the Raman spectrum of monolayer graphene, bilayer graphene, and bulk graphite." Physical Review B 77(24).

Du, X., I. Skachko, et al. (2008). "Approaching ballistic transport in suspended graphene." Nature Nanotechnology 3(8): 491-495.

Eizenberg, M. and J. M. Blakely (1979). "Carbon Monolayer phase condensation on Ni(111) " Surface Science 82: 228-236.

Ferrari, A. C., J. C. Meyer, et al. (2006). "Raman Spectrum of Graphene and Graphene Layers." Physical Review Letters 97(18): 187401.

Forbeaux, I., J.-M. Themlin, et al. (1998). "Heteroepitaxial graphite on 6H-SiC(0001): Interface formation through conduction-band electronic structure." Physical Review B 58(24): 16396-16406.

Geim, A. K. and K. S. Novoselov (2007). "The rise of graphene." Nat Mater 6(3): 183-191.

Gilje, S., S. Han, et al. (2007). "A Chemical Route to Graphene for Device Applications." Nano Letters 7(11): 3394-3398.

Gomez De Arco, L., Y. Zhang, et al. "Continuous, Highly Flexible, and Transparent Graphene Films by Chemical Vapor Deposition for Organic Photovoltaics." ACS Nano 4(5): 2865-2873.

Gomez, L., Y. Zhang, et al. (2009). "Synthesis, Transfer and Devices of Single- and Few-Layer Graphene by Chemical Vapor Deposition." IEEE Transactions on Nanotechnology 8(2): 135-138.

Gupta, A., G. Chen, et al. (2006). "Raman Scattering from High-Frequency Phonons in Supported n-Graphene Layer Films." Nano Letters 6(12): 2667-2673.

Han, M. Y., Ouml, et al. (2007). "Energy Band-Gap Engineering of Graphene Nanoribbons." Physical Review Letters 98(20): 206805.

Hayes, B. (2005). "Why W?" American Scientist 93: 104-108.

Hwang, E. H., S. Adam, et al. (2007). "Transport in chemically doped graphene in the presence of adsorbed molecules." Physical Review B 76(19): 195421.

Li, X., W. Cai, et al. (2009). "Large-Area Synthesis of High-Quality and Uniform Graphene Films on Copper Foils." Science 324(5932): 1312-1314.

Lin, Y.-M., K. A. Jenkins, et al. (2008). "Operation of Graphene Transistors at Gigahertz Frequencies." Nano Letters 9(1): 422-426.

Lin, Y. M., C. Dimitrakopoulos, et al. "100-GHz Transistors from Wafer-Scale Epitaxial Graphene." Science 327(5966): 662-.

Meric, I., N. Baklitskaya, et al. (2008). "RF performance of top-gated, zero-bandgap graphene field-effect transistors." Ieee International Electron Devices Meeting 2008, Technical Digest: 513-516.

Mermin, N. D. (1968). "Crystalline Order in Two Dimensions." Physical Review 176(1): 250.

Moon, J. S., D. Curtis, et al. (2009). "Epitaxial-Graphene RF Field-Effect Transistors on Si-Face 6H-SiC Substrates." Electron Device Letters, IEEE 30(6): 650-652.

Novoselov, K. S., A. K. Geim, et al. (2004). "Electric Field Effect in Atomically Thin Carbon Films." Science 306: 666-669.

Ortiz-Conde, A., F. J. García Sánchez, et al. (2000). "Exact analytical solutions of the forward non-ideal diode equation with series and shunt parasitic resistances." Solid-State Electronics 44(10): 1861-1864.

Peumans, P., A. Yakimov, et al. (2003). "Small molecular weight organic thin-film photodetectors and solar cells." Journal of Applied Physics 93(7): 3693-3723.

Reina, A., X. T. Jia, et al. (2009). "Large Area, Few-Layer Graphene Films on Arbitrary Substrates by Chemical Vapor Deposition." Nano Letters 9(1): 30-35.

Shelton, J. C., H. R. Patil, et al. (1974). "Equilibrium segregation of carbon to a nickel (111) surface: A surface phase transition." Surface Science 43(2): 493-520.

Somani, P. R., S. P. Somani, et al. (2006). "Planer nano-graphenes from camphor by CVD." Chemical Physics Letters 430: 56-59

Tung, V. C., L.-M. Chen, et al. (2009). "Low-Temperature Solution Processing of Graphene#Carbon Nanotube Hybrid Materials for High-Performance Transparent Conductors." Nano Letters 9: 1949–1955.

Viculis, L. M., J. J. Mack, et al. (2003). "A Chemical Route to Carbon Nanoscrolls." Science 299: 1361.

Wu, J., H. A. Becerril, et al. (2008). "Organic solar cells with solution-processed graphene transparent electrodes." Applied Physics Letters 92: 263302.1-263302.3.

Wu, Z., Z. Chen, et al. (2004). "Transparent, Conductive Carbon Nanotube Films." Science 305: 1273-1276.

Yu, H., J. B. Li, et al. (2003). "Two- versus three-dimensional quantum confinement in indium phosphide wires and dots." Nature Materials 2(8): 517-520.

Yu, Q., J. Lian, et al. (2008). "Graphene segregated on Ni surfaces and transferred to insulators." Applied Physics Letters 93, : 113103.1-113103.3.

Zhang, Y., L. Gomez, et al. "Comparison of Graphene Growth on Single-Crystalline and Polycrystalline Ni by Chemical Vapor Deposition." The Journal of Physical Chemistry Letters 1(20): 3101-3107.

Zhang, Y., Y.-W. Tan, et al. (2005). "Experimental observation of the quantum Hall effect and Berry's phase in graphene." Nature 438: 201-204.

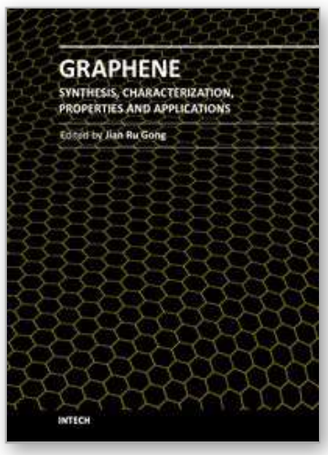

Graphene - Synthesis, Characterization, Properties and Applications

Edited by Prof. Jian Gong

ISBN 978-953-307-292-0
Hard cover, 184 pages
Publisher InTech
Published online 15, September, 2011
Published in print edition September, 2011

The discovery of graphene has led to a deluge of international research interest, and this new material in the field of materials science and condensed-matter physics has revealed a cornucopia of new physics and potential applications. This collection gives a roughly review on the recent progress on the synthesis, characterization, properties and applications of graphene, providing useful information for researchers interested in this area.

How to reference

In order to correctly reference this scholarly work, feel free to copy and paste the following:

Lewis Gomez De Arco, Yi Zhang and Chongwu Zhou (2011). Large Scale Graphene by Chemical Vapor Deposition: Synthesis, Characterization and Applications, Graphene - Synthesis, Characterization, Properties and Applications, Prof. Jian Gong (Ed.), ISBN: 978-953-307-292-0, InTech, Available from: http://www.intechopen.com/books/graphene-synthesis-characterization-properties-and-applications/large-scale-graphene-by-chemical-vapor-deposition-synthesis-characterization-and-applications

INTECH
open science | open minds

InTech Europe
University Campus STeP Ri
Slavka Krautzeka 83/A
51000 Rijeka, Croatia
Phone: +385 (51) 770 447
Fax: +385 (51) 686 166
www.intechopen.com

InTech China
Unit 405, Office Block, Hotel Equatorial Shanghai
No.65, Yan An Road (West), Shanghai, 200040, China
中国上海市延安西路65号上海国际贵都大饭店办公楼405单元
Phone: +86-21-62489820
Fax: +86-21-62489821

IntechOpen